MRS Communications (2021) 11:189–196

https://doi.org/10.1557/s43579-021-00033-z

MRS Communications

Polymers for Additive Manufacturing Research Letter

Effect of micron-scale manufacturing flaws on the tensile response of centimeter sized two-photon polymerization microlattices

Jean-Baptiste Forien, James S. Oakdale, Matthew A. Worthington, Juergen Biener, Materials Science Division, Lawrence Livermore National Laboratory, Livermore 94550, USA

Address all correspondence to Jean-Baptiste Forien at **forien1@llnl.gov**

(Received 24 November 2020; accepted 25 March 2021; published online 15 April 2021)

Abstract

Two-photon polymerization (TPP) is a unique fabrication technique that enables sub-micron scale resolution. Herein, we report on uniaxial tensile tests on millimeter-sized TPP log-pile structures that were fabricated using a recently developed interdigitated stitching strategy. As expected, the Young's modulus increased with laser intensity, however elastic modulus, ultimate strength and strain-at-failure varied widely, even for nominally identical samples. Post-mortem analysis revealed a series of print defects resulting from various sources including misalignments, resin shrinkage, laser beam shadowing, and local depletion of the oxygen inhibitor. While some of the defects can be eliminated, such as misalignments due to insufficient precision of the mechanical stage, others are more intrinsic to TPP and thus more difficult to address.

Introduction

Two photon polymerization (TPP) is a laser direct-writing manufacturing technique that enables rapid fabrication of three-dimensional (3D) objects with features as small as 100 nm.[1] TPP relies on a tightly focused pulsed laser to induce multi-photon absorption and initiate local polymerization chemistries. Arbitrarily complex structures can be formed by moving the focal point of the laser within the volume of photoresin using motion stages, laser scanners or combination thereof. Galvo mirrors are often deployed to facilitate high speed fabrication, reaching writing speeds up to several centimeters per second,[2] which is a prerequisite for time-efficient printing of macroscopic parts with nanometer resolution. However, galvo scanning has its limitations, primarily due to aberration, distortion and vignetting effects that restrict the print field. Therefore, larger objects printed via galvo mirrors require the use of a motion stage to stitch individual write fields together.[3,4] We have observed systemic failures along stitch seams that complicate handling and integration of TPP low-density materials into functional devices (e.g. high energy density laser targets). Herein, we assess the mechanical properties of mm-scale log-pile lattices with sub-micron features under uniaxial tensile stress.

TPP low density parts can be readily derived from lattice sub-units and have found use in a variety of applications ranging from metamaterials[5] to laser targets.[4,6–8] Stitching of galvo-scanning derived lattice blocks to form macroscopic parts can result in mechanical weak stitch seams due to misalignments of the beams across stitch seams. This renders the final part prone to mechanical failure by catastrophic fracture.[4] To address this problem, new stitching concepts have been developed including adaptive stitching techniques that optimize and reduce the total amount of stitched blocks for a given object geometry[9] or physically constrained stitching based on stitching jigsaw puzzle shaped blocks together.[4] However, these stitching methods still involve printing adjacent blocks next to each other and thus do not address the problem of misaligned beams across seams that causes mechanically weak stitching interfaces. Recently, we proposed a solution by using an interdigitated approach where adjacent log-pile lattice blocks are printed with 50% overlap, see Fig. 1(a).[4] Although misalignment still results in flaws along the stitch seams, the seams are constrained within the interdigitated sub-lattice which strengthens the structure.

Previous work studied the effect of printing defects on the mechanical response of TPP-fabricated nanostructures.[10–12] However, the complexity involved with handling micro-sized TPP objects constitutes a considerable challenge and limits the choice of experimentation. Testing of TPP parts thus has traditionally relied on uniaxial compression tests. Notable examples of defect testing by compression include; examination of surface flaws that deteriorate the fracture resistance of hollow ceramic unit-cell lattice,[13] or investigation of missing ligaments that reduce Young's modulus of engineered lattices.[12] Generally, tensile tests on porous materials are more sensitive towards the presence of defects than compression tests: in tensile tests, stress concentration caused by the presence of a defect trigger catastrophic failure of the sample; in compression tests, defects cause local densification that stabilizes the defect region. Therefore, tensile tests of low-density materials that require handling of the sample are much more challenging than compression tests. Uniaxial tensile testing on single voxel lines

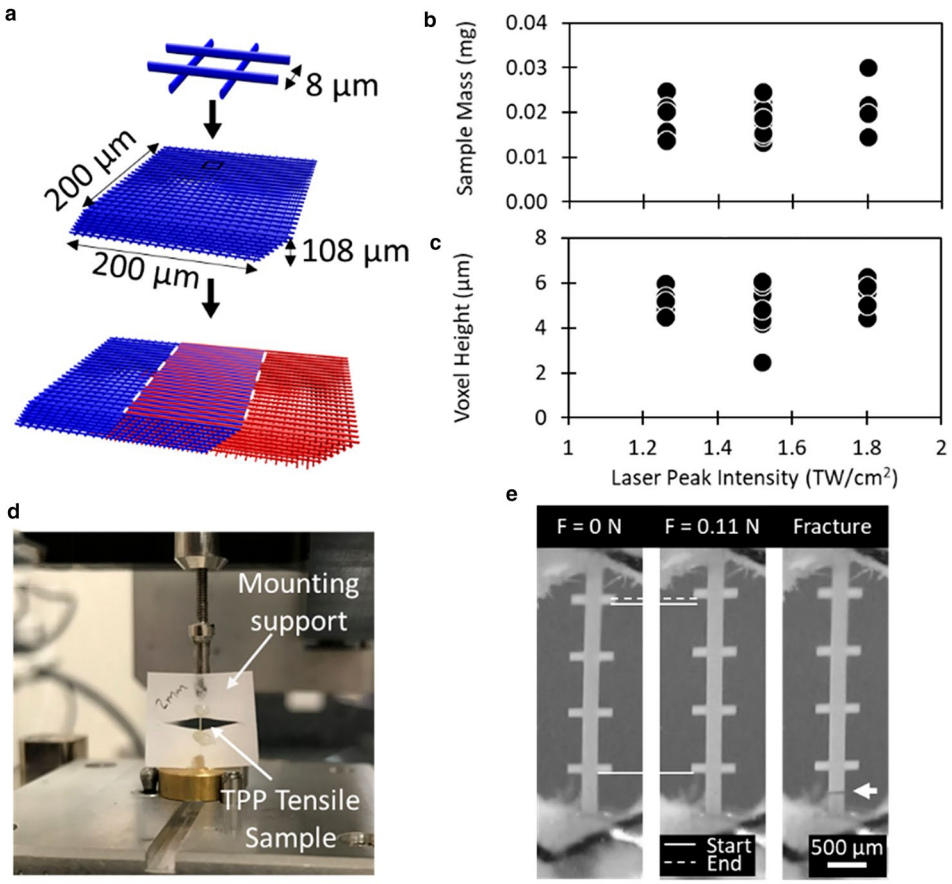

Figure 1. Log-pile tensile test structures manufactured using TPP lithography. (a) Schematic representation of lines of voxels, forming the core element of the log-pile structure. Lines are printed parallel to each other with 8 µm gap and with every other layer being perpendicular to the previous layer. Layers of lines form a single block of 200 × 200 × 108 µm^3. To eliminate shadowing, aberration and vignetting effects we use a 60 degree slanted block design. Blocks of log-piles are printed with 50% overlap to homogenize the distribution of possible misalignments throughout the volume of the built object. Plots of sample mass (b) and voxel's height (c) *vs*. laser peak intensity used for printing. (d) Picture of the tensile test experimental setup showing the glued TPP samples on the diamond paper cut support and (e) video frames of the tensile test sample in the unloaded state (left), and at maximum strain before (center) and after fracture (right). The solid and dashed white lines indicates the position of the top and bottom marker blocks in the unloaded state and at peak strain, respectively.

has recently been demonstrated using MEMs devices[14] and push-to-pull structures.[15] Tensile experimentation on unit-cell lattice containing defined notches exhibited an increase in elastic modulus from horizontal to vertical notches.[16] In a similar uniaxial tensile experiment, change of mechanical behavior was observed in polymer lattices with high- and low-density structures revealing brittler and ductile mechanical responses, respectively.[17]

In this work, we investigated the mechanical properties of mesoscale TPP log-pile structures under tensile stress. Strain was monitored through both image correlation and motion of the tensile test stage. While the tensile tests confirmed the expected increase in Young's modulus with increasing laser power, we observe large variations in the mechanical response of nominally identical samples. The heterogeneity of the load–displacement results is discussed in terms of print defects resulting from various sources including misalignment of the sub-lattices in interdigitated log-pile structures due to of the lower precision of the mechanical stage, resin shrinkage, laser beam shadowing, and local depletion of the oxygen inhibitor.

Materials and methods

Two photon polymerization samples were prepared using a Nanoscribe GmbH Photonic Professional GT laser lithography system. A FemtoFiber pro NIR laser (Topica, Photonics LLC, Milpitas, CA, USA), operating at a wavelength of 780 nm, a pulse duration (τ) of 100 fs and a repetition rate (f) of 80 MHz, was focused with a Zeiss Plan-Neofluar 25×/0.8 IMM Corr Ph2 M27 objective. Transmittance (T) at 780 nm was 0.8, as reported by the manufacturer. Average laser power (P, mW) was measured before the microscope objective and was varied to control light exposure. Laser peak intensity (I, TW cm^{-2}) was

recalculated from the following equation: $I=(2PT)/(f\omega 2\pi\tau)$, where ω (beam waist) $=0.61\lambda/\mathrm{NA}$.

Tensile test specimens were printed using the "dip-in laser lithography" mode[18] with IP-DIP (Nanoscribe GmbH) photoresist applied to a glass slide substrate ($25\times25\times0.7$ mm^3). The log-pile test samples (3.8 mm long, 200 μm wide and 108 μm high) were created using an interdigitated stitching protocol in which individual log-pile blocks ($200\times200\times108$ μm^3) with 8 μm XY spacing and 4 μm Z spacing were stitched together by tiling with 50% overlap and 60° slant angle [Fig. 1(a)]. The two overlapping sub-lattices were offset by half of the *x*/*y* lattice constant resulting in a nominal 4 μm log-pile spacing. Additional unit blocks were printed orthogonally to the sample length to allow tracking of the deformation during tensile test experiments. Positioning of each unit-cell printing location was done by motorized stage translations at a linear velocity rate of 250 μm s^{-1}, and the unit-cells were printed using galvanometer scanning with a 10 mm s^{-1} speed. A total number (n) of 15 samples was manufactured with 1.26 TW cm^{-2} ($n=3$), 1.52 TW cm^{-2} ($n=8$), and 1.80 TW cm^{-2} ($n=4$) peak laser intensity.

Substrates containing the printed samples were sequential immersed in propylene glycol monomethyl ether acetate (1 h) and isopropyl alcohol (0.2 h). The samples were then UV-cured under 3 mW 365 nm UV light in a 0.02 M isopropyl alcohol solution containing 2,2-dimethoxy-2-phenylacetophenone.[6,19] Finally, the samples were transferred to a bath of acetone and CO_2 supercritical point dried using an EMS (electron microscopy sciences) 3100 dryer. The samples were weighed using a Mettler XPSU Ultra micro-balance, and the results of the mass measurement are summarized in Fig. 1(b). Scanning electron micrographs of the samples were obtained after tensile test experiments with a Phenom Pro desktop scanning electron microscope (SEM) at an accelerating voltage of 10 keV. All samples were sputter coated with 5 nm Au prior to SEM imaging. Voxel heights of the samples were measured from the SEM images and are showed in Fig. 1(c).

A custom-made tensile test setup comprised of a high-precision weighing sensor (WM124-L22, Mettler Toledo, Columbus OH, USA) and stepper motor actuator (conex-TRB6CC, Newport, Irvine, CA, USA) was used to perform uniaxial tensile tests. Initially, and for ease of handling, the ends of the samples were glued with epoxy (Hardman Double Bubble Red Extra Fast Setting Epoxy) on a paper support structure with a diamond shape cutout. The paper support was then cut along the long axis of the sample thereby freeing the sample to absorb the entire tensile load during testing. The paper/sample assembly was carefully transferred to the testing apparatus and the paper supports were tacked onto the tensile tester grips using a UV-curable epoxy [Fig. 1(d)]. In retrospective, the sample ends could have been directly glued on two separate pieces of paper to avoid the delicate paper cutting step. Experiments were performed with a deformation velocity of 50 μm s^{-1} and data acquisition rate every 0.1 s. Tensile stage control as well as data acquisition was carried out using custom LabView script. A Canon EOS 5d Mark II Digital SLR camera equipped with a Canon EF 100 mm f/2.8 Macro USM lens was used to record sample deformation during tests with a frame rate of 30 images per seconds and effective resolution of $\sim10\times10$ μm^2 per pixel [Fig. 1(e)].

Stress values were obtained by dividing the force applied on the weight sensor by the cross-sectional area of samples. Strain values were derived from the actuator's controller and verified by tracking the positions of satellite blocks from video frames to correct for the compliance of the sample holder/support paper.

Results and discussion

Stress–strain curves derived from uniaxial tensile-tests of interdigitated TPP samples [Fig. 2(a)] show a linear elastic regime that is either directly ended by brittle fracture or followed by a short elastic–plastic regime characterized by a decreasing slope before final failure. Overall, the stress–strain curves indicate a brittle behavior of the lattice samples with, in some cases, limited plastic deformation. The corresponding Young' modulus calculated at 0.2% of strain shows an increase of the average elastic modulus with increasing laser power, from 163 ± 73 MPa to 279 ± 161 MPa, and 404 ± 36 MPa for 1.26, 1.52 and 1.80 TW cm^{-2} peak laser intensity, respectively [Fig. 2(b)]. This increase agrees with results from other mechanical studies performed on unit-block[20–22] and single voxel-line objects.[23,24] The increase of the modulus was attributed to higher degrees of conversion and larger voxel cross-sectional dimensions resulting from increased light intensity. In our case, we did not observe a significant change in voxel height [Fig. 1(c)] or weight [Fig. 1(b)] as a functional of laser peak intensity. The log-pile lattices under investigation in this study were designed to have nominal density of 0.2 g cm^{-3} realized by a design with a XY-log spacing of 4 μm and a Z-spacing between planes of 4 μm. Lattices printed with intensities <1.25 TW cm^{-2} collapsed during development resulting in both densification and density inhomogeneities. We attribute the collapse at lower laser intensities to under-sized voxels resulting in poor Z-plane interconnectivity, which exacerbates the bend-dominated failure mechanism of log-pile structures. The insensitivity of voxel growth towards the intensity profiles used herein, 1.26 to 1.8 TW cm^{-2}, are likely a result of operating near the upper resolution limit of the objective, such that the change in voxel size would be minimal, while the degree of conversion can be anticipated to increase.

Although a trend in Young's modulus was observed, nominally identical samples vary widely, specifically for the 1.52 TW cm^{-2} samples with modulus values that scatter from 50 to 250 MPa [Fig. 2(b)]. The same is true for the ultimate tensile strength data [Fig. 2(c)]: while the average values of the ultimate tensile strength slightly increases with increasing laser power, the range of ultimate tensile strength data measured for nominally identical samples is larger than the effect caused by increasing laser power. The data also shows no correlation

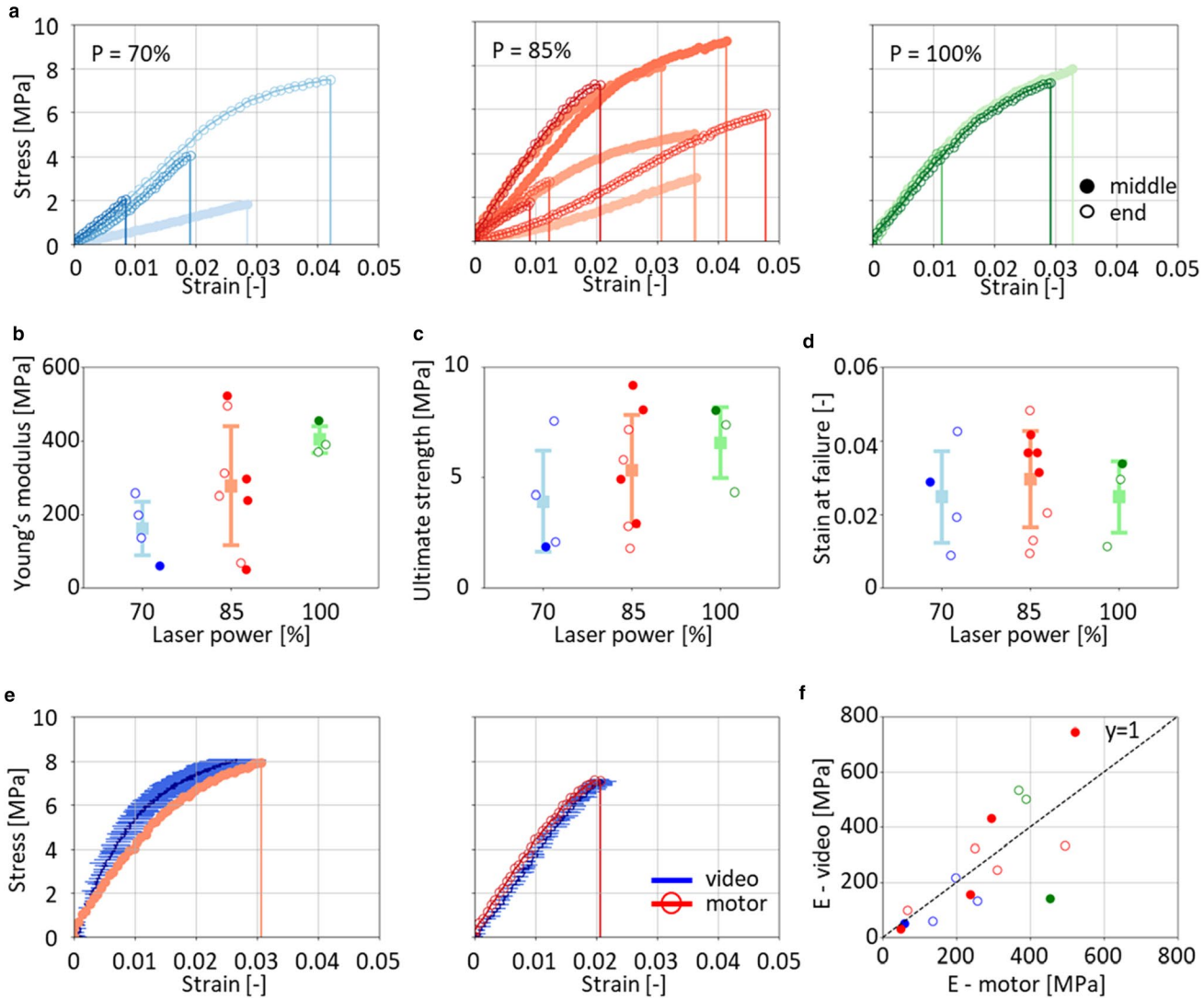

Figure 2. (a) Stress–strain curves of uniaxially loaded two photon polymerization samples, with strain derived from motor position. Log-pile samples were printed with 1.26, 1.52 and 1.80 TW cm^{-2} laser peak intensity. Plots of properties derived from the stress–strain curves are represented with regards to laser power such as (b) Young's modulus calculated at 0.02% strain, (c) ultimate tensile strength and (d) strain at failure for the different laser power. (e) Stress–strain curves of the samples with strain calculated with digital image correlation performed on videos taken during tensile experiments. (f) Plot of strain at failure values from digital image correlation vs. strain at failure derived from the motorize stage. Samples were pulled until fracture, which occurred either in the middle or at the end of the tensile bar, represented in all panels with full and empty circle, respectively.

between the strain-at-failure and peak laser intensity [Fig. 2(d)]. Even nominally identical samples fail at very different strain values, ranging from no plastic deformation to 3–5% strain. For example, one sample printed at 1.26 TW cm^{-2} deforms even more than any of its counterparts printed with 1.80 TW cm^{-2}. Finally, we attempted to test non-interdigitated, otherwise identical log-pile samples, but repeatedly encountered pre-mature fracture failures during specimen handling and mounting.

To check if the scatter in the data for the interdigitated samples is caused by variations in the compliance of sample stage/sample mounting, we compared the stress–strain curves [Fig. 2(e)] and the strain values at failure [Fig. 2(f)] derived from the sample stage motion with those from image correlation. The image correlation analysis was performed by tracking the positions of the satellite blocks printed with periodic spacing along each sample. For most of the samples we find good agreement between the two strain values [Fig. 2(e)] thus ruling out stage/sample mounting compliance issues as reason for the large scatter of the data. Image correlation also reveals that the strain is relatively evenly distributed along the tensile test samples, indicated by the small standard deviation in strain [Fig. 2(e)], which corresponds to the contribution of strain values from all satellite's combinations.

Next, we investigated the appearance and location of fracture surfaces. SEM inspection of the fracture surface of the samples suggests that crack initiation and propagation, leading

to fracture, occurs randomly [Fig. 3(a)] without preference for stitch lines [Fig. 3(b)]. This observation suggests that the interdigitation strategy effectively mitigates the mechanical weakness of stitch lines. Thus, neither stage/sample mounting compliance issues [Fig. 2(e), (f)] nor stitch interface effects (Fig. 3) seem to explain the large variation of the mechanical response of nominally identical samples [Fig. 2(a)].

Misalignment of the two sub-lattice structures constitute another possible defect responsible for the mechanical response of TPP structures. Misalignments can be caused by the low accuracy of motorized stage, anisotropic motion/shrinkage effects, and laser beam shadowing. The misalignments of the interdigitated blocks caused by the limited accuracy of the motorized stage can be observed when looking at top [Fig. 4(a)] and side-views [Fig. 4(b)] of the samples. It should be noted that these misalignments varied randomly across the length of the test specimen, with some areas exhibiting little to no misalignment. Side-view SEM images further revealed various line spacing lattice flaws [Fig. 4(b)]. Like the top-down images in Fig. 4(a), there is a clear misalignment of the two interdigitated sub-lattices (color coded in red and blue as guide the eye) and this is again partly ascribed to stage-induced misalignments. However, a slight variation in the degree of this misalignment can be observed from top to bottom. The print design is represented in Fig. 4(c) with schematic illustration of the misalignment defects in Fig. 4(d). We believe this variation is due to a combination of anisotropic motion/shrinkage effects induced by rigid substrate constraints, such that the top of the lattice is able to undergo a greater degree of motion relative to the bottom portion directly attached to the substrate. Forces that could be anticipated to induce motion would include shear from viscous fluid flow as a result of dragging the objective through the resign during DIP-In printing, as well as intrinsic volume shrinkage as the acrylate functional groups react and cure.[25] Finally, on close inspection it became apparent that the interdigitated sub-lattice (blue lines) fades, and almost entirely disappears, from top to bottom [Fig. 4(e)]. We hypothesize that this defect is a direct result of so-called shadowing effects caused by optical aberrations of laser beam traversing through cured resin (i.e. interdigitated sub-lattices).[26] The refractive index of acrylate systems is known to vary as function of the degree of cure,[27] and the degree of conversion is also well known to increase with greater dosage.[23] Thus, structures fabricated with higher peak laser intensities will exhibit greater refractive index changes enhancing the likely hood of distortions. This issue can be circumvented by printing shorter blocks or lattices with higher porosity.

It is important to note that these types of misalignments also effects ligaments running along the long axis of the samples. In the extreme case, complete misalignment of the adjacent sub-lattices (that is, the sublattices are printed directly on top of each other rather than with the intended 4 μm offset) would reduce the number of load bearing ligaments along the sample axis, and thus the Young's modulus by a factor of two.

Finally, adding to the complexity, webbing defects were present in all the 1.80 TW cm^{-2} samples and some, but not all, of the 1.26 and 1.52 TW cm^{-2} specimen [Fig. 4(f)]. These webbing defects are a result of proximity effects arising from depletion of intrinsic radical inhibitors (i.e. molecular oxygen and quinone stabilizers)[4] and appear as a fine fractal-structure primarily found at the center of the unit-cell block and therefore easily missed by surface imaging techniques such as electron microscopy. We do not anticipate that this webbing material contributed significantly to the observed mechanical properties, as the observed insensitivity of the sample weight on increasing peak laser intensity indicates that the mass added by webbing defects can be neglected.

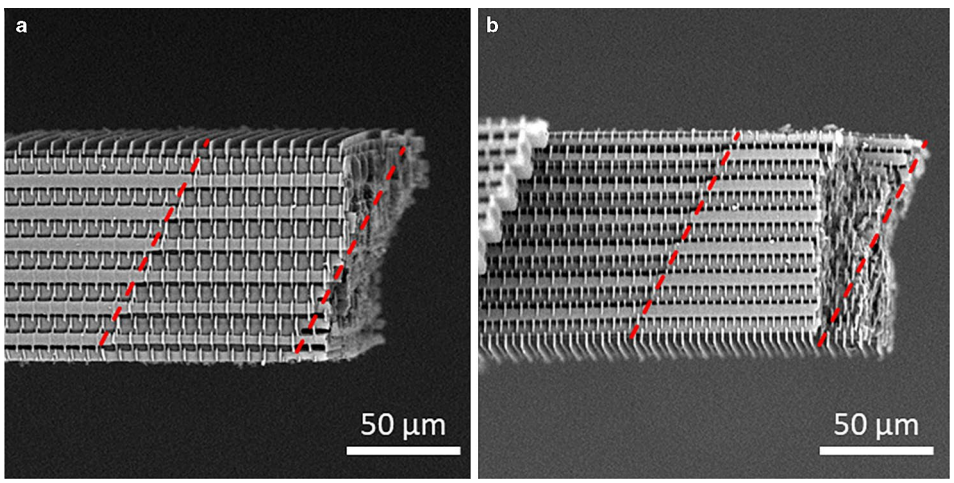

Figure 3. SEM images of interdigitated log-pile samples. Side views of fractured samples indicate that crack propagated both (a) between and (b) at stitch interfaces. The red dashed lines are guides for the eye, representing stitch seams occurring every 100 μm for overlapping blocks.

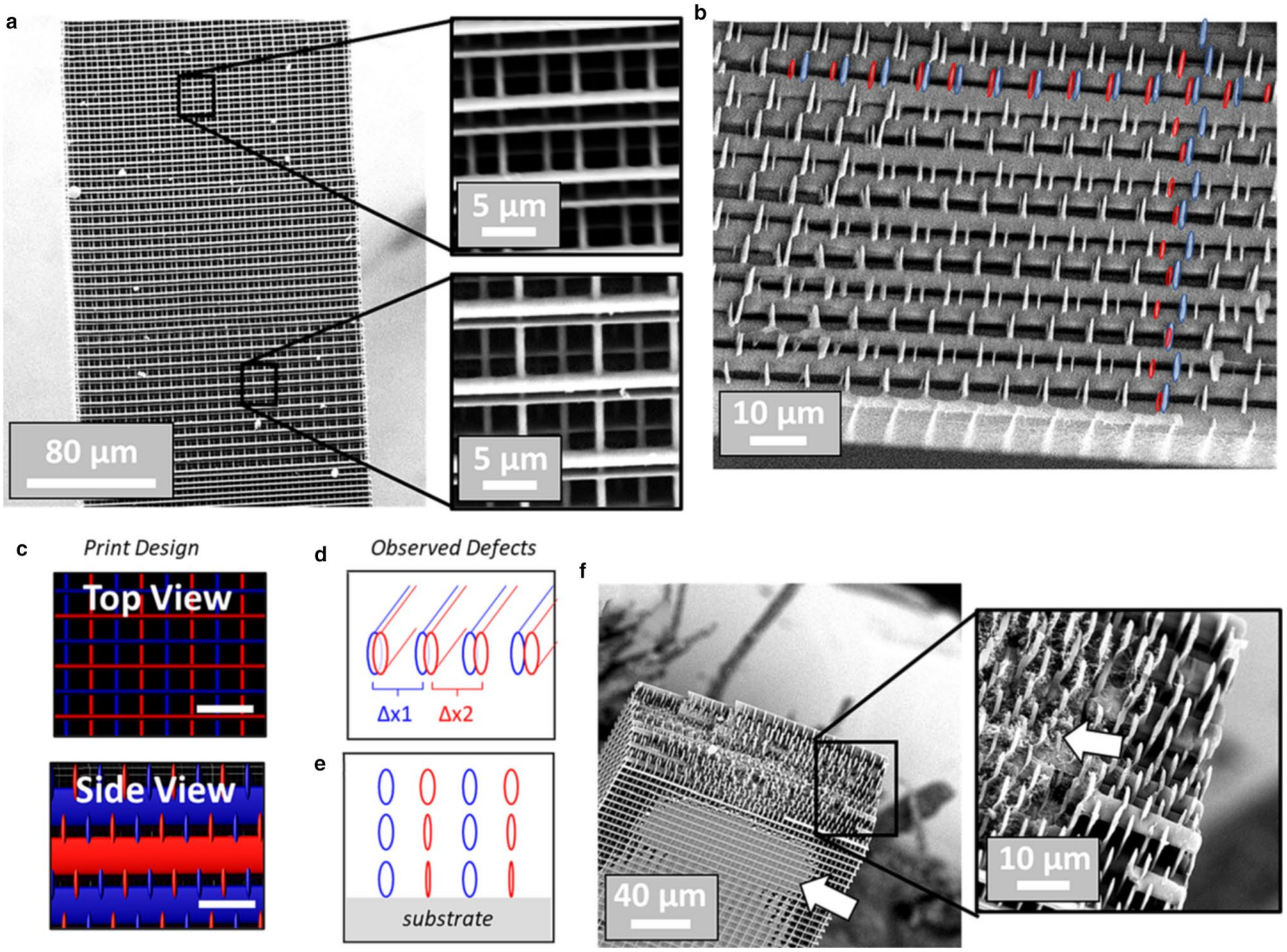

Figure 4. TPP printing defects: (a) top-view SEM image of a stitch interface showing the overlap and misalignment of two adjacent sub-lattice unit-blocks. (b) Side view of samples showing that spacing between the lines of the two sub-lattices varies vertically as well as and horizontally. The red and blue ovals indicate different sub-lattices. (c) Schematic of print design containing even spacing between logs of the two sub-lattices. Scalebar equals 8 µm (d) Schematic representation of spacing variations between to sub-lattices. (e) Schematic illustration of log-pile dimensions gradient of the second sub-lattice toward the substrate. (f) Cross-sectional SEMs revealing the presence of webbing defects in some of the samples.

Conclusion

In summary, we performed tensile tests on millimeter-sized TPP log-pile structures that were printed using an optimized interdigitated stitching design. This stitching design was very effective in eliminating the typically observed stitch interface dominated failure of millimeter-sized low density TPP samples as evidenced by the robustness of our samples during handling, and the observation that our tensile test specimens failed with equal probability at and in between stitch lines. However, while we observed an average increase of Young's modulus with increasing laser power, the large spread in standard deviation makes it difficult to predict the mechanical properties of such structures. The values for the Young's modulus, ultimate strength, and strain-at-failure all varied widely even for nominally identically samples. The poor reproducibility of the millimeter-sized samples in terms of mechanical properties is surprising as the printing is digitally controlled and thus expected to offer high reproducibility. Thus, our results suggest that the macroscopic mechanical properties of these low-density materials are dominated by defects.

As main defects we identified the misalignment of the log-pile blocks caused by photoresist shrinkage and limited precision of the mechanical stage. Specifically, the latter could affect the number of load bearing ligaments and thus of the Young's modulus by as much as a factor of two. Another identified defect that could affect the mechanical behavior was a systematic variation of voxel size and shape within the second sub-lattice of the interdigitated log-pile structure which can be attributed to changes of the refractive index while printing the first sub-lattice block. Finally, webbing effects were observed in the center of the blocks of some samples, but again even nominally identical samples differed in this defect.

So while the interdigitated print design allows the fabrication of macroscopic mechanically robust low-density samples

that can be easily handled and integrated into functional devices, it does not result in predictable mechanical properties, at least under tensile stress where the mechanical behavior is dominated by print defects.

While some of the defects like photoresist-shrinkage-induced misalignment are intrinsic to TPP and difficult to address, others like misalignment due to insufficient precision of the mechanical stage can be addressed by hardware and/or software upgrades. Hardware upgrades like installing higher precision mechanical stage directly address the root problem but may be difficult to realize in an existing commercial system. Among software upgrades, in situ image registration between prescribed and printed part seems to be especially promising as it enables in situ correction of the print process. However, the effectiveness of this approach depends on the available image resolution and thus also may require additional hardware upgrades. In situ image registration also is computationally expensive and may slow down the print process. Alternatively, one could imagine adopting a new printing modality, such as tiling individual blocks by synchronizing the galvanometer scanner with continuous movement of the XY translation stage. This would allow printing of larger parts but requires feedback from both device and controller.

The hardware and software improvements discussed above ideally should also be supplemented by resin optimization. For example, resins with lower curing shrinkage or higher transparency may help to reduce misalignment issues and morphological gradients. Formulating stronger and stiffer resins will generally benefit print quality. Finally, developing lattice designs that are less sensitive towards misalignment is another promising avenue. Towards this end, we started to explore herringbone and chevron-like patterns which are less sensitive towards ligament misalignments but also change the ligament deformation mode from stretching to bending dominated. More fracture tolerant lattice designs can also be realized by adopting more compliant sinewave or helicoidal ligaments designs.

Acknowledgments

The work was performed under the auspices of the US Department of Energy by LLNL under Contract No. DE-AC52-07NA27344. The project was supported by the Laboratory Directed Research and Development (LDRD) programs of LLNL (18-ERD-004).

Data availability

The datasets generated during and/or analyzed during the current study are available from the corresponding author on reasonable request.

Declarations

Conflict of interest

On behalf of all authors, the corresponding author states that the authors have no financial or proprietary interests in any material discussed in this article

References

1. X. Zhou, Y. Hou, J. Lin, A review on the processing accuracy of two-photon polymerization. *AIP Adv.* **5**, 030701 (2015)
2. V. Hahn, P. Kiefer, T. Frenzel, J. Qu, E. Blasco, C. Barner-Kowollik, M. Wegener, Rapid assembly of small materials building blocks (voxels) into large functional 3D metamaterials. *Adv. Funct. Mater.* **30**, 1907795 (2020)
3. Y. Liu, O. Stein, J. H. Campbell, L. Jiang, N. Petta, and Y. Lu, Three-dimensional printing and deformation behavior of low-density target structures by two-photon polymerization. *Nanoeng. Fabr. Prop. Opt. Devices XIV* **10354** (2017).
4. J.S. Oakdale, R.F. Smith, J.-B. Forien, W.L. Smith, S.J. Ali, L.B.B. Aji, T.M. Willey, J. Ye, A.W. van Buuren et al., Direct laser writing of low-density interdigitated foams for plasma drive shaping. *Adv. Funct. Mater.* **27**, 1702425 (2017)
5. T. Frenzel, M. Kadic, M. Wegener, Three-dimensional mechanical metamaterials with a twist. *Science* **358**, 1072–1074 (2017)
6. L.J. Jiang, J.H. Campbell, Y.F. Lu, T. Bernat, N. Petta, direct writing target structures by two-photon polymerization. *Fusion Sci. Technol.* **70**, 295–309 (2016)
7. Y. Liu, J.H. Campbell, O. Stein, L. Jiang, J. Hund, Y. Lu, Deformation behavior of foam laser targets fabricated by two-photon polymerization. *Nanomaterials* **8**, 498 (2018)
8. O. Stein, Y. Liu, J. Streit, J.H. Campbell, Y.F. Lu, Y. Aglitskiy, N. Petta, Fabrication of low-density shock-propagation targets using two-photon polymerization. *Fusion Sci. Technol.* **73**, 153–165 (2018)
9. S. Dehaeck, B. Scheid, P. Lambert, Adaptive stitching for meso-scale printing with two-photon lithography. *Addit. Manuf.* **21**, 589–597 (2018)
10. A. Gross, P. Pantidis, K. Bertoldi, S. Gerasimidis, Correlation between topology and elastic properties of imperfect truss-lattice materials. *J. Mech. Phys. Solids* **124**, 577–598 (2019)
11. L.R. Meza, A.J. Zelhofer, N. Clarke, A.J. Mateos, D.M. Kochmann, J.R. Greer, Resilient 3D hierarchical architected metamaterials. *Proc. Natl. Acad. Sci.* **112**, 11502–11507 (2015)
12. B.M. Patterson, L. Kuettner, T. Shear, K. Henderson, M.J. Herman, A. Ionita, N. Chawla, J. Williams, T. Sun et al., Synchrotron CT imaging of lattice structures with engineered defects. *J. Mater. Sci.* **55**, 11353 (2020)
13. D. Jang, L.R. Meza, F. Greer, J.R. Greer, Fabrication and deformation of three-dimensional hollow ceramic nanostructures. *Nat. Mater.* **12**, 893–898 (2013)
14. D.R. Cayll, I.S. Ladner, J.H. Cho, S.K. Saha, M.A. Cullinan, A MEMS dynamic mechanical analyzer for in situ viscoelastic characterization of 3D printed nanostructures. *J. Micromech. Microeng.* **30**, 075008 (2020)
15. J. Bauer, A. Schroer, R. Schwaiger, I. Tesari, C. Lange, L. Valdevit, O. Kraft, Push-to-pull tensile testing of ultra-strong nanoscale ceramic–polymer composites made by additive manufacturing. *Extreme Mech. Lett.* **3**, 105–112 (2015)
16. A.J. Mateos, W. Huang, Y.-W. Zhang, J.R. Greer, Discrete-continuum duality of architected materials: failure, flaws, and fracture. *Adv. Funct. Mater.* **29**, 1806772 (2019)
17. A.R. Garcia-Taormina, T. Juarez, J.S. Oakdale, J. Biener, A.M. Hodge, Scaling-up of nano-architected microstructures: a mechanical assessment. *Adv. Eng. Mater.* **21**, 1900687 (2019)
18. T. Bückmann, N. Stenger, M. Kadic, J. Kaschke, A. Frölich, T. Kennerknecht, C. Eberl, M. Thiel, M. Wegener, Tailored 3D mechanical metamaterials made by dip-in direct-laser-writing optical lithography. *Adv. Mater.* **24**, 2710–2714 (2012)

19. J.S. Oakdale, J. Ye, W.L. Smith, J. Biener, Post-print UV curing method for improving the mechanical properties of prototypes derived from two-photon lithography. *Opt. Express* **24**, 27077–27086 (2016)
20. L.J. Jiang, Y.S. Zhou, W. Xiong, Y. Gao, X. Huang, L. Jiang, T. Baldacchini, J.-F. Silvain, Y.F. Lu, Two-photon polymerization: investigation of chemical and mechanical properties of resins using Raman microspectroscopy. *Opt. Lett.* **39**, 3034–3037 (2014)
21. E.D. Lemma, F. Rizzi, T. Dattoma, B. Spagnolo, L. Sileo, A. Qualtieri, M. De Vittorio, F. Pisanello, Mechanical properties tunability of three-dimensional polymeric structures in two-photon lithography. *IEEE Trans. Nanotechnol.* **16**, 23–31 (2017)
22. C.-S. Shin, T.-J. Li, C.-L. Lin, Alleviating distortion and improving the Young's modulus in two-photon polymerization fabrications. *Micromachines* **9**, 615 (2018)
23. J. Bauer, A.G. Izard, Y. Zhang, T. Baldacchini, L. Valdevit, Programmable mechanical properties of two-photon polymerized materials: from nanowires to bulk. *Adv. Mater. Technol.* **4**, 1900146 (2019)
24. I.S. Ladner, M.A. Cullinan, S.K. Saha, Tensile properties of polymer nanowires fabricated via two-photon lithography. *RSC Adv.* **9**, 28808–28813 (2019)
25. Y. He, M. Yao, J. Nie, Shrinkage in UV-Curable Coatings. in *Prot. Coat. Film Form. Prop.*, eds. by M. Wen, K. Dušek (2017)
26. L. Jonušauskas, M. Malinauskas, Mesoscale 3D manufacturing: varying focusing conditions for efficient direct laser writing of polymers. in *Nanophotonics V* **9126** (2014)
27. J.B. Mueller, J. Fischer, F. Mayer, M. Kadic, M. Wegener, Polymerization kinetics in three-dimensional direct laser writing. *Adv. Mater.* **26**, 6566–6571 (2014)